

Citation for published version:

Abbaszadeh, H, Souslov, A, Paulose, J, Schomerus, H & Vitelli, V 2017, 'Sonic Landau Levels and Synthetic Gauge Fields in Mechanical Metamaterials', *Physical Review Letters*, vol. 119, no. 19, 195502, pp. 1-6.
<https://doi.org/10.1103/PhysRevLett.119.195502>

DOI:

[10.1103/PhysRevLett.119.195502](https://doi.org/10.1103/PhysRevLett.119.195502)

Publication date:

2017

Document Version

Peer reviewed version

[Link to publication](#)

(C) 2017 American Physical Society.

University of Bath

Alternative formats

If you require this document in an alternative format, please contact:
openaccess@bath.ac.uk

General rights

Copyright and moral rights for the publications made accessible in the public portal are retained by the authors and/or other copyright owners and it is a condition of accessing publications that users recognise and abide by the legal requirements associated with these rights.

Take down policy

If you believe that this document breaches copyright please contact us providing details, and we will remove access to the work immediately and investigate your claim.

Sonic Landau levels and synthetic gauge fields in mechanical metamaterials

Hamed Abbaszadeh,¹ Anton Souslov,^{1,2} Jayson Paulose,¹ Henning Schomerus,³ and Vincenzo Vitelli^{1,2,*}

¹*Instituut-Lorentz, Universiteit Leiden, Leiden 2300 RA, The Netherlands*

²*The James Franck Institute and Department of Physics,
The University of Chicago, Chicago, IL 60637, USA*

³*Department of Physics, Lancaster University, Lancaster LA1 4YB, United Kingdom*

(Dated: September 18, 2018)

Mechanical strain can lead to a synthetic gauge field that controls the dynamics of electrons in graphene sheets as well as light in photonic crystals. Here, we show how to engineer an analogous synthetic gauge field for lattice vibrations. Our approach relies on one of two strategies: shearing a honeycomb lattice of masses and springs or patterning its local material stiffness. As a result, vibrational spectra with discrete Landau levels are generated. Upon tuning the strength of the gauge field, we can control the density of states and transverse spatial confinement of sound in the metamaterial. We also show how this gauge field can be used to design waveguides in which sound propagates with robustness against disorder as a consequence of the change in topological polarization that occurs along a domain wall. By introducing dissipation, we can selectively enhance the domain-wall-bound topological sound mode, a feature that may potentially be exploited for the design of sound amplification by stimulated emission of radiation (SASERs, the mechanical analogs of lasers.)

Electronic systems subject to a uniform magnetic field experience a wealth of fascinating phenomena such as topological states [1] in the integer quantum Hall effect [2] and anyons associated with the fractional quantum Hall effect [3]. Recently, it has been shown that in a strained graphene sheet, electrons experience external potentials that can mimic the effects of a magnetic field, which results in the formation of Landau levels and edge states [4, 5]. Working in direct analogy with this electronic setting, pseudo-magnetic fields have been engineered by arranging CO molecules on a gold surface [6] and in photonic honeycomb-lattice metamaterials [7, 8].

In this article, we apply insights about wave propagation in the presence of a gauge field to acoustic phenomena in a nonuniform phononic crystal, using the appropriate mechanisms of strain-phonon coupling and frictional dissipation, in contrast to those present in electronic and photonic cases. The acoustic metamaterial context in which we implement gauge fields provides us with significant control [9–11] over frequency, wavelength, and attenuation scales unavailable in the analogous electronic realizations. For example, a metamaterial composed of stiff (e.g., metallic) components of micron-scale length may be suitable for control over ultrasound with gigahertz-scale frequencies, whereas cm-scale metamaterials may provide control over kHz-scale sound waves. We develop two strategies for realizing a uniform pseudo-magnetic field in a metamaterial based on the honeycomb lattice, i.e., “mechanical graphene” [12]. In the first strategy, we apply stress at the boundary to obtain nonuniform strain in the bulk, which leads to a Landau-level spectrum, whereas in the second strategy, we exploit built-in, nonuniform patterning of the local metamaterial stiffness. This second strategy shows how the unique controllability of metamaterials can lead to novel designs inac-

cessible in the electronic context, and may be useful in scaling up these phenomena to long acoustic waveguides.

We explore acoustic phenomena associated with the Landau-level spectrum. For example, the acoustic analog of Shubnikov-de Haas oscillations [13] corresponds to a sharp peak in the phonon density of states at the Landau-level frequency. In addition, sound modes are confined within a length scale set by the analog of the magnetic length. Even stronger confinement of sound modes can be engineered at a domain wall associated with a change in the effective mass of the phononic excitations, which localizes phonon modes that are analogous to the topological domain-wall states in the Su-Schrieffer-Heeger model of polyacetylene [14]. We show how this domain-wall-bound mode exhibits robustness against a type of disorder that may come in the manufacturing of acoustic metamaterials—disorder in the stiffness of each component. Like other realizations of topological states [15, 16] in mechanical [17–27], acoustic [28–36], and photonic [37] metamaterials, this characterization may help with the design of robust devices. We show that introducing dissipation on just one of the two sublattices enhances the domain-wall-bound sound mode. This feature may be implemented in the acoustic context using a material immersed in a viscous fluid (appropriate for low-Reynolds number, e.g., micro-scale metamaterials), or by including dampers (e.g., small dashpot dampers at every components for cm-scale realizations) within the material design. We suggest this feature may be exploited for the design of acoustic couplers, rectifiers, and sound amplification by stimulated emission of radiation (SASERs).

Mechanical graphene. We begin with a minimal, microscopic model of an acoustic metamaterial—a set of nodes positioned at the vertices of a honeycomb lattice and connected by rods to their nearest neighbors (see

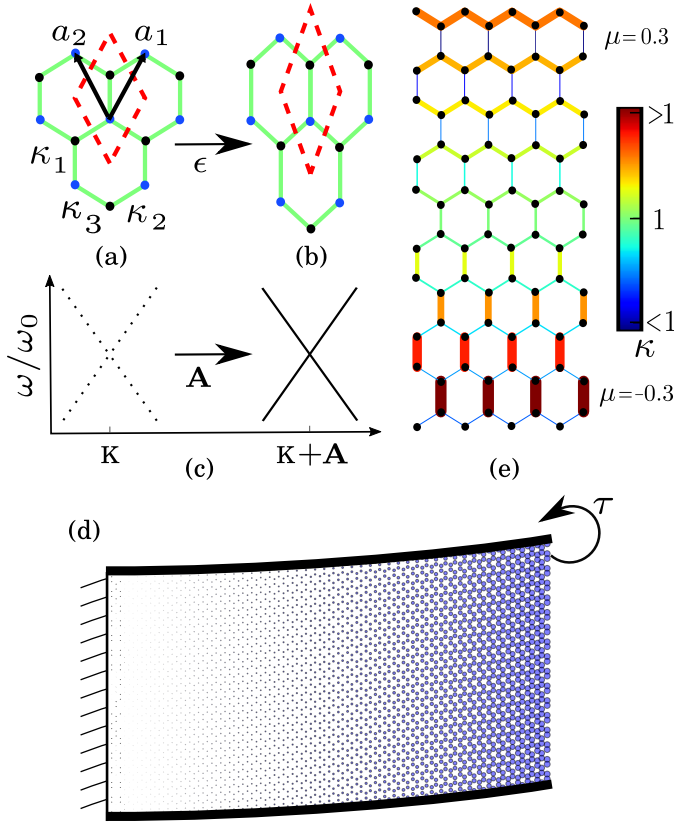


FIG. 1: (a) Mechanical graphene—a set of rods and nodes based on the honeycomb structure. The dashed line indicates the shape of a unit cell. (b) The lattice with a pure shear strain. (c) The shift of a Dirac point within the phonon spectrum of mechanical graphene due to the applied strain can be used to define an effective vector potential. (d) An externally applied nonuniform pure shear deformation that corresponds to a constant magnetic field. The external stress is applied by a torque τ on the boundary rods. (e) A non-uniform patterning of the local material stiffness that leads to a constant magnetic field. We consider periodic boundary conditions along x and free boundary conditions along y .

Fig. 1a) [12]. The compressional stiffness of the rods κ is determined by their fixed Young's modulus E , variable cross-section area S , and length a via ES/a . We assume the rods to be so slender that their bending stiffness is significantly lower than their compressional stiffness. We model the rods as central-force harmonic springs, whose elastic energy U is given in terms of the strain $\delta r/a$ by $U(\delta r) = \frac{1}{2}\kappa(|\mathbf{r} + \delta\mathbf{r}| - a)^2$. For small strains, this energy can be linearized in terms of node displacements \mathbf{u}_1 and \mathbf{u}_2 as $U(\mathbf{u}_1, \mathbf{u}_2) = \frac{1}{2}\kappa(\mathbf{e} \cdot [\mathbf{u}_1 - \mathbf{u}_2])^2$, where $\mathbf{e} \equiv \mathbf{r}/|\mathbf{r}|$ is the unit vector along the spring. (In Fig. 1a, we define the initial configuration for the node positions and stiffnesses.) Given this potential, we examine the linear equation of motion for acoustic vibrations of the lattice:

$$-m\ddot{u}_i^\alpha = \frac{\partial U}{\partial u_i^\alpha} = \sum_{j,\beta} D_{ij}^{\alpha\beta} u_j^\beta, \quad (1)$$

where u_i^α are the $\alpha = x, y$ components of displacement of the i th site and $D_{ij}^{\alpha\beta}$ are components of the dynamical matrix. In a periodic lattice, the solutions to this equation of motion are plane waves $\mathbf{u}_{\mathbf{q}} e^{i(\omega(\mathbf{q})t - \mathbf{q} \cdot \mathbf{x})}$, where both the dispersion relation $\omega(\mathbf{q})$ and the normal modes $\mathbf{u}_{\mathbf{q}}$ are found from the corresponding eigenvalue problem for each wavevector \mathbf{q} .

To lowest order in perturbation theory around point K [defined by $\mathbf{q}_K \equiv (0, 4\pi/3\sqrt{3}a)$], the dynamical matrix for the two bands near the frequency $\omega_0 \equiv \sqrt{3\kappa/2m}$ reduces to [38]

$$D = -\frac{1}{2}\omega_0^2(a\delta\mathbf{q} + \mathbf{A}) \cdot \boldsymbol{\sigma} + (1 + V)\omega_0^2\mathbb{I}, \quad (2)$$

where \mathbb{I} is the 2×2 identity matrix, $\delta\mathbf{q} \equiv \mathbf{q} - \mathbf{q}_K$, and $\boldsymbol{\sigma} \equiv (\sigma_x, \sigma_y)$ contains Pauli spin matrices. The gauge field \mathbf{A} and potential V are both zero for the homogeneous honeycomb lattice. From the structure of Eq. (2), we note that the dispersion around \mathbf{q}_K has the form of a Dirac cone, i.e., two bands touch at the Dirac point [39].

Synthetic gauge field. We now proceed to show that unlike uniform lattice deformations that merely shift this Dirac cone in wavevector space, nonuniform deformations can lead to an effective synthetic gauge field for sound. For uniform strain (Fig. 1b), \mathbf{A} and V are both constant throughout the lattice. On the other hand, for a nonuniform but slowly varying strain, the position of the local Dirac point varies from one region to another (Fig. 1c), which corresponds to spatially dependent fields \mathbf{A} and V . In terms of the affine component \mathbf{U} and nonaffine component \mathbf{W} of the displacement denoting, respectively, common and relative displacements of the two sublattices,

$$\mathbf{A}(x, y) = a(\mathbf{q}_K \cdot \nabla)\mathbf{U} + 3(\epsilon_{ps}, -\epsilon_{xy}) + (W_y, -W_x)/a,$$

and $V = \frac{1}{2} \text{Tr } \epsilon$, where $\epsilon_{ij} \equiv (\partial_i U_j + \partial_j U_i)/2$ is the linear affine strain and $\epsilon_{ps} \equiv (\epsilon_{xx} - \epsilon_{yy})/2$ is its pure shear component.

To simplify the design of an acoustic device based on this strained lattice, we now consider those lattice strains that can be obtained by applying forces only on the boundary. Such a configuration requires that the forces in the bulk of the material balance each other. In the material we consider, this force-balance condition is satisfied provided that the nonaffine displacements depend on the affine strain via $W_x = \epsilon_{xy}a$ and $W_y = \epsilon_{ps}a$. Thus, we obtain the following expression for the gauge field in a boundary-strained material:

$$\mathbf{A}(x, y; \epsilon) = a(\mathbf{q}_K \cdot \nabla)\mathbf{U} + 4(\epsilon_{ps}, -\epsilon_{xy}). \quad (3)$$

For acoustic systems, we can also follow a second strategy: patterning the local material stiffness to achieve a spatially dependent gauge field \mathbf{A} . For example, we can smoothly vary the composition or thickness of the rods to change their effective spring constants to $\kappa_i = \kappa + \delta\kappa_i$,

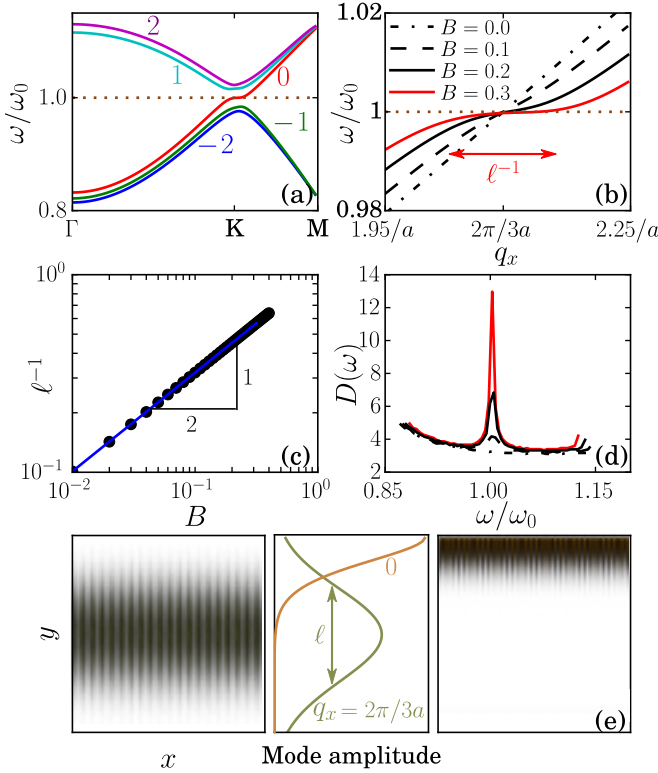


FIG. 2: Mechanical Landau levels: (a) A pseudo-magnetic field leads to Landau levels around the Dirac point. (b) As the magnetic field increases, the zeroth-Landau-level band flattens. Band flatness can be characterized by the inverse magnetic length ℓ^{-1} . (c) The inverse magnetic length scales as the square root of the magnetic field. (d) Density of states for the zeroth Landau level, for the same values of B as in (b). The peak at the Dirac frequency rises as the bands flatten. (e) Visualizations of the zeroth Landau level at two different wavevectors. For $\mathbf{q} = \mathbf{q}_K$, this mode has a Gaussian profile around the waveguide center, whereas far from this point, at $\mathbf{q} = 0$, the mode decays exponentially away from the edge.

where $i = 1 \dots 3$ labels springs in the lattice unit cell. We find that the gauge field and potential are given by

$$\mathbf{A}(x, y; \delta\kappa) = \left(-\frac{1}{3} \frac{2\delta\kappa_1 + \delta\kappa_2 + \delta\kappa_3}{\kappa}, \frac{\delta\kappa_2 - \delta\kappa_3}{\sqrt{3}\kappa} \right),$$

$$V = \frac{\delta\kappa_1 + \delta\kappa_2 + \delta\kappa_3}{3\kappa}. \quad (4)$$

To obtain a Landau-level spectrum, we select \mathbf{A} and V such that (for units in which $a = 1$)

$$\nabla \times \mathbf{A} = B\hat{z} = \text{const}; \quad V = 0. \quad (5)$$

For any selection satisfying the conditions of Eqs. (5), the dynamical matrix in Eq. (2) has the form of the Hamiltonian for a Dirac electron in a plane with a constant magnetic field B applied perpendicular to that plane [40, 41]. Let us now consider two practical solutions to Eqs. (5): (i) an externally applied nonuniform pure shear deformation, and (ii) nonuniform patterning of the spring constants along the y -direction.

For case (i), we find the particle displacements throughout the lattice by substituting Eq. (3) into Eqs. (5) and solving the resulting partial differential equation: $\partial_y U_x + \partial_x U_y = -Bx/2$, with the additional constraint $\partial_x U_x = \partial_y U_y = 0$, which corresponds to non-volumetric pure shear deformations. The resulting displacements satisfy: $U_x = 0$ and $U_y = -Bx^2/4$. Note that for the honeycomb lattice, this condition can be realized using the boundary stresses illustrated in Fig. 1d.

For case (ii), we substitute Eqs. (4) into Eqs. (5) to find the condition $\sqrt{3}\partial_x(\delta\kappa_2 - \delta\kappa_3) - \partial_y(\delta\kappa_2 + \delta\kappa_3) = 3\kappa B$ for the spatial dependence of the spring constants. We consider a material uniform along the x -direction. This condition is satisfied for spring constants given by

$$\mu \equiv \frac{\delta\kappa_2}{\kappa} = \frac{\delta\kappa_3}{\kappa} = -\frac{\delta\kappa_1}{2\kappa} = \frac{By}{3}, \quad (6)$$

which is visualized in Fig. 1e.

Mechanical Landau levels. Now that we have proposed metamaterial architectures that realize the acoustic analog of a constant magnetic field, we go on to explore the physical consequences of this field for sound waves. To proceed, we focus on an architecture that is peculiar to the acoustic context, i.e., we select the realization of a patterned metamaterial waveguide described by Eqs. (6). Such a quasi-one-dimensional waveguide is uniform along the x -axis, graded along the y -axis, and is subject to no-stress boundary conditions on its top and bottom (see Fig. 1e). The constant pseudo-magnetic field leads to a Landau-level spectrum for frequencies near ω_0 (Fig. 2a).

Let us focus on the acoustic band corresponding to the most prominent Landau level: $n = 0$. In Fig. 2b, this band is plotted for several values of the pseudo-magnetic field B ; as the pseudo-magnetic field increases, the band flattens over a larger region in wavevector space, which leads to an increasing peak in the density of acoustic states (Fig. 2d). The width of this flat region defines an inverse length scale ℓ^{-1} , which scales as $\ell^{-1} \sim \sqrt{B/a}$ (Fig. 2c). This length scale is the acoustic analog of the magnetic length in a Landau level [39]. An acoustic mode in a Landau level has a Gaussian profile with a transverse confinement given by ℓ (Fig. 2e). The transverse location of this mode within the waveguide is controlled by the mode wavenumber q_x , in contrast to an index-graded waveguide in which the location is determined by mode frequency. Consequently, in our case, the location of sound at a targeted frequency can be significantly tuned via the mode wavenumber (Fig. 2e and [39]).

Sublattice-polarized domain wall modes. The $n = 0$ Landau level at $q_x = q_{K,x} \equiv 2\pi/3a$ has frequency ω_K , is located at the waveguide center, and involves displacements exclusively on one sublattice. Modes with these properties generically appear in regions across which A_x changes sign, i.e., their local dispersions have Dirac cones on opposite sides of point K . As an example, we consider a waveguide with two domain walls that separate

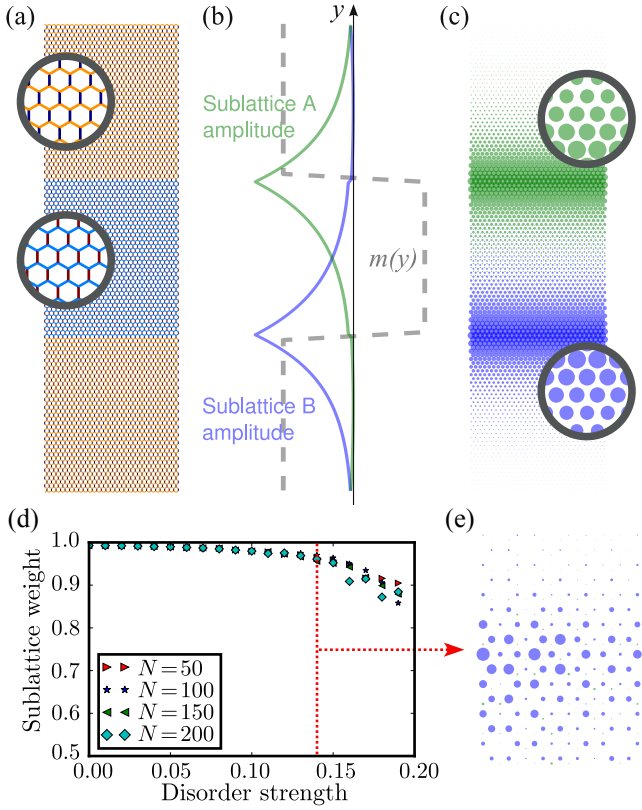


FIG. 3: (a) Waveguide with two domain walls separating two regions with $\mu = 0.08$ from a central region with $\mu = -0.08$. Bonds are colored according to their spring constants as in Fig. 1e. Periodic boundary conditions are applied along x . (b) Variation of the effective Dirac mass $m(y)$ (dashed line) and midgap-mode amplitude for $q_x = 2\pi/3a$ on either sublattice (solid lines). (c) Visualization of midgap mode with sublattices distinguished, showing strong sublattice polarization. Each point on the A (B) sublattice is represented by a green (blue) disc whose area is proportional to the amplitude of the midgap mode. (d) Sublattice polarization of the domain-wall-bound mode in the presence of disorder in the spring constants [39]. (e) Even in the presence of strong (14%) disorder, we observe sublattice polarization due to the topological origin of the mode.

a uniform central region with spring constants set by $\mu = -0.08$ from two regions, one above and one below, that each have $\mu = 0.08$ (Fig. 3a). At $q_x = q_{K,x}$, the spectrum as a function of q_y near point K is described by a gapped 1D Dirac Hamiltonian centered about ω_K , with effective mass proportional to A_x [39]. The “spin” degree of freedom corresponds to the two sublattices of the honeycomb lattice: eigenstates of σ_z with eigenvalue ± 1 involve displacements solely on one sublattice. When the mass $m(y)$ varies spatially, domain walls at which $m(y)$ changes sign harbor exponentially localized midgap modes that are “spin-polarized”, i.e., confined to a single sublattice [14, 42]. The sublattice on which the mode is localized is determined by the sign of the change in mass upon crossing the domain wall. Fig. 3b–c shows

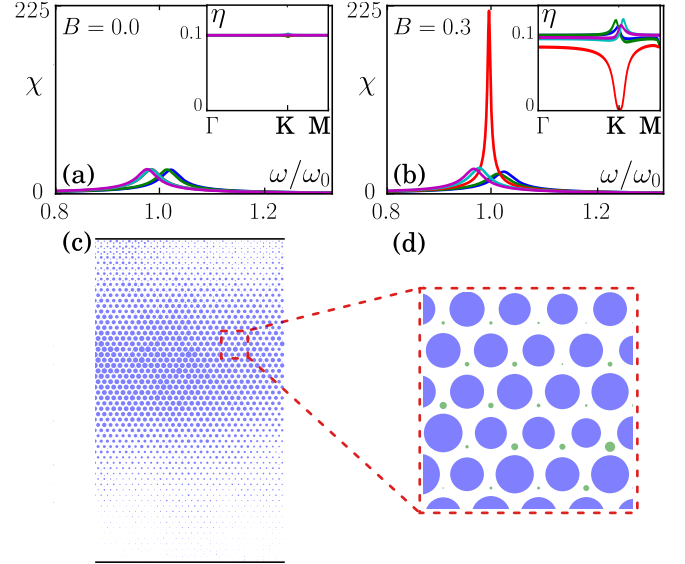


FIG. 4: Single-mode response χ of Landau-level states in mechanical graphene, including the effect of damping on one sublattice and for pseudo-magnetic field values (a) $B = 0.0$ and (b) $B = 0.3$. Colors correspond to the different Landau-level bands identified in Fig. 2a. Insets: wavenumber-dependent attenuation rate η of the corresponding bands. (c) The steady-state response (for $B = 0.3$) to external periodic forcing with frequency close to the Dirac frequency and at an edge that is situated 50 unit cells to the left of the section shown. Each point is represented by a disc whose area is proportional to the amplitude of the response. (d) Zoom-in of (c) shows that the Landau-level mode is selectively enhanced due to the presence of sublattice-biased damping.

the numerically-obtained midgap mode for the domain wall geometry in Fig. 3a, whose components on sublattice A (B) fall off exponentially from the top (bottom) domain wall. The robustness of the sublattice polarization under disorder in the spring constants is shown in Fig. 3d–e and is explained in the SI [39].

Selective enhancement. The sublattice polarization of the Landau-level states can be used to selectively enhance these modes under external drive by employing site-dependent damping. For example, for positive magnetic fields, the Landau-level states live only on the A-sublattice of the honeycomb unit cell [4, 40]. If we introduce damping of the form $-\gamma \dot{\mathbf{u}}_B$ into the equation of motion, Eq. (1), such that only the displacements of the B-sublattice are damped, then the Landau-level acoustic waves would not be attenuated, whereas the rest of the sound waves, which generically are split between the A and B sublattices, would have a nonzero attenuation [39]. To characterize this selective enhancement, we study the attenuation rate $\eta(\mathbf{q})$ as a function of mode wavevector, as well as the self-response function $\chi(\omega)$ which measures the displacements in response to a drive at frequency ω [39]. In Fig. 4a–b, we plot $\chi(\omega)$ and $\eta(\mathbf{q})$ for the Landau-level bands with $-2 \leq n \leq 2$, in response

to an oscillatory drive that is proportional to the corresponding mode displacement vector. In the absence of the pseudo-magnetic field B , the response is underdamped, but no mode stands out as having a largest peak in χ (Fig. 4a), whereas for nonzero B , χ exhibits a strong peak at a frequency ω_0 , corresponding to the zeroth Landau-level (Fig. 4b). Therefore, when an edge of the metamaterial is driven near ω_0 , the pseudo-magnetic field combined with selective damping leads to selective enhancement of acoustic Landau-level modes (Fig. 4c–d) relative to the rest of the attenuated acoustic spectrum.

Towards mechanical lasers. This phenomenon is the acoustic analog of selective enhancement of microwave modes realized in Ref. [43]. Just as selective enhancement for light waves may lead to the design of novel parity-time-symmetric [44, 45] and topological [8] lasers, analogously, selective enhancement of sound waves may be useful in the design of sound amplification by stimulated emission of radiation (SASERs), i.e., the acoustic analog of lasers, acoustic couplers and rectifiers. The design of such devices [46] would involve acoustic resonators, acoustic drive, and nonlinearity of response. A potential architecture for this device may involve resonators at every node in the metamaterial, with an external acoustic source populating the states within each resonator.

Note added. After our work was submitted, we learned about Ref. [47] that examines Landau levels in metamaterials composed of acoustic resonant cavities.

Acknowledgments. We gratefully acknowledge funding from FOM, NWO, and Delta Institute for theoretical physics (H.A., A.S., J.P., and V.V.) and from EPSRC Programme Grant No. EP/N031776/1 (H.S.).

H.A. and A.S. contributed equally to this work.

* Electronic address: vitelli@uchicago.edu

- [1] C. L. Kane and E. J. Mele, Phys. Rev. Lett. **95**, 146802 (2005).
- [2] M. Z. Hasan and C. L. Kane, Rev. Mod. Phys. **82**, 3045 (2010).
- [3] R. B. Laughlin, Phys. Rev. Lett. **50**, 1395 (1983).
- [4] F. Guinea, M. I. Katsnelson, and A. K. Geim, Nature Phys. **6**, 30 (2010).
- [5] N. Levy, S. A. Burke, K. L. Meaker, M. Panlasigui, A. Zettl, F. Guinea, A. H. Castro Neto, and M. F. Crommie, Science **329**, 544 (2010).
- [6] K. K. Gomes, W. Mar, W. Ko, F. Guinea, and H. C. Manoharan, Nature **483**, 306 (2012).
- [7] M. C. Rechtsman, J. M. Zeuner, A. Tünnermann, S. Nolte, M. Segev, and A. Szameit, Nature Photonics, **7**, 153 (2013).
- [8] H. Schomerus and N. Y. Halpern, Phys. Rev. Lett. **110**, 013903 (2013).
- [9] L. Wu and L. Chen, J. App. Phys. **110**, 114507 (2011).
- [10] F. Casadei, T. Delpero, A. Bergamini, P. Ermani, and M. Ruzenne, J. App. Phys. **110**, 013903 (2012).
- [11] K. H. Matlack, M. Serra-Garcia, A. Palermo, S. D. Huber, and C. Daraio, arXiv:1612.02362, (2016).
- [12] T. Kariyado and Y. Hatsugai, Sci. Rep. **5**, 18107 (2015).
- [13] L. Shubnikov and W. J. de Haas, Comm. Phys. Lab. Univ. Leiden, **207a** (1930).
- [14] W. P. Su, J. R. Schrieffer, and A. J. Heeger, Phys. Rev. Lett. **42**, 1698 (1979).
- [15] E. Prodan and C. Prodan, Phys. Rev. Lett. **103**, 248101 (2009).
- [16] N. Berg, K. Joel, M. Koolyk, and E. Prodan, Phys. Rev. E **83**, 021913 (2011).
- [17] C. L. Kane and T. C. Lubensky, Nature Phys. **10**, 39 (2013).
- [18] H. C. Po, Y. Bahri, and A. Vishwanath, Phys. Rev. B **93**, 205158 (2016).
- [19] B. G. Chen, N. Upadhyaya, and V. Vitelli, Proc. Natl. Acad. Sci. USA **111**, 13004 (2014).
- [20] L. M. Nash, D. Kleckner, A. Read, V. Vitelli, A. M. Turner, and W. T. M. Irvine, Proc. Natl. Acad. Sci. USA **112**, 1449 (2015).
- [21] J. Paulose, B. G. Chen, and V. Vitelli, Nature Phys. **11**, 153 (2015).
- [22] J. Paulose, A. S. Meeussen, and V. Vitelli, Proc. Natl. Acad. Sci. USA **112**, 7639 (2015).
- [23] D. Z. Rocklin, B. G. Chen, M. Falk, V. Vitelli, and T. C. Lubensky, Phys. Rev. Lett. **116**, 135503 (2016).
- [24] D. Z. Rocklin, S. Zhou, K. Sun, and X. Mao, Nature Comm. **8**, 14201 (2017).
- [25] R. Süssstrunk and S. D. Huber, Science, **349**, 47 (2015).
- [26] B. G. Chen, B. Liu, A. A. Evans, J. Paulose, I. Cohen, V. Vitelli, and C. D. Santangelo, Phys. Rev. Lett. **116**, 135501 (2016).
- [27] A. S. Meeussen, J. Paulose, and V. Vitelli, Phys. Rev. X **6**, 041029 (2016).
- [28] A. B. Khanikaev, R. Fleury, S. H. Mousavi, and A. Alù, Nature Comm. **6**, 8260 (2015).
- [29] Z. Yang, F. Gao, X. Shi, X. Lin, Z. Gao, Y. Chong, and B. Zhang, Phys. Rev. Lett. **114**, 114301 (2015).
- [30] P. A. Deymier, K. Runge, N. Swintek, and K. Muralidharan, Comptes Rendus - Mecanique **343**, 700 (2015).
- [31] S. H. Mousavi, A. B. Khanikaev, and Z. Wang, Nature Comm. **6**, 8682 (2015).
- [32] Y. T. Wang, P. G. Luan, and S. Zhang, New J. Phys. **17**, 73031 (2015).
- [33] P. Wang, L. Lu, and K. Bertoldi, Phys. Rev. Lett. **115**, 104302 (2015).
- [34] M. Xiao, W. J. Chen, W. Y. He, and C. T. Chan, Nature Phys. **11**, 920 (2015).
- [35] R. Süssstrunk and S. D. Huber, Proc. Natl. Acad. Sci. USA **113**, E4767 (2016).
- [36] C. Brendel, V. Peano, O. Painter, and F. Marquardt, arXiv:1607.04321, (2016).
- [37] L. Lu, J. D. Joannopoulos, and M. Soljačić, Nature Comm. **6**, 6710 (2015).
- [38] Near the point K' ($\mathbf{q}_{K'} = -\mathbf{q}_K$), the analogous expression differs only by $\mathbf{A} \rightarrow -\mathbf{A}$.
- [39] See Supplementary Information [url] for further explanations, which includes Ref. [48].
- [40] R. Jackiw, Phys. Rev. D **29**, 2375 (1984).
- [41] G. W. Semenoff, Phys. Rev. Lett. **53**, 2449 (1984).
- [42] R. Jackiw and C. Rebbi, Phys. Rev. D **13**, 3398 (1976).
- [43] C. Poli, M. Bellec, U. Kuhl, F. Mortessagne, and H. Schomerus, Nature Comm. **6**, 6710 (2015).
- [44] H. Hodaie, M. Miri, M. Heinrich, D. N. Christodoulides,

- and M. Khajavikhan, *Science* **346**, 975 (2014).
- [45] Liang Feng, Zi Jing Wong, Ren-Min Ma, Yuan Wang, and Xiang Zhang, *Science* **346**, 972 (2014).
- [46] I. Mahboob, K. Nishiguchi, F. Fujiwara, and H. Yamaguchi, *Phys. Rev. Lett.* **110**, 127202 (2013).
- [47] Z. Yang, F. Gao, Y. Yang, and B. Zhang, *Phys. Rev. Lett.* **118**, 194301 (2017).
- [48] C. Herring, *Phys. Rev.* **52**, 365 (1937).

SUPPLEMENTARY INFORMATION FOR “SONIC LANDAU LEVELS AND SYNTHETIC GAUGE FIELDS IN MECHANICAL METAMATERIALS”

Here, we provide derivations for Eqs. (3, 5) of the main text, the domain-wall-localized modes, and selective enhancement.

Synthetic gauge fields for strain and patterning

In a periodic material, the equations of motion (1) admit plane-wave solutions $\mathbf{u} = \mathbf{u}_{\mathbf{q}} e^{i(\omega(\mathbf{q})t - \mathbf{q} \cdot \mathbf{x})}$ associated with the eigenvalue problem $D(\mathbf{q})\mathbf{u}_{\mathbf{q}} = m\omega_{\mathbf{q}}^2 \mathbf{u}_{\mathbf{q}}$, where the dynamical matrix of the two-dimensional honeycomb lattice is:

$$D(\mathbf{q}) = \frac{1}{m} \sum_{\alpha=1}^3 \kappa_{\alpha} \begin{pmatrix} P_{\alpha} & -P_{\alpha} e^{i\mathbf{q} \cdot \boldsymbol{\delta}_{\alpha}} \\ -P_{\alpha} e^{-i\mathbf{q} \cdot \boldsymbol{\delta}_{\alpha}} & P_{\alpha} \end{pmatrix}, \quad (\text{S1})$$

where $P_{\alpha} = \mathbf{e}_{\alpha} \mathbf{e}_{\alpha}^T$. Of the four bands of this dynamical matrix, two of them are degenerate at the Dirac point. Using first-order perturbation theory around the Dirac point, we find the following form for the dynamical matrix projected onto the two Dirac bands:

$$D_0 = -\frac{3\kappa}{4m} a \delta \mathbf{q} \cdot \boldsymbol{\sigma} + \frac{3\kappa}{2m} \mathbb{I}, \quad (\text{S2})$$

where $\boldsymbol{\sigma} \equiv (\sigma_x, \sigma_y)$, which involves the Pauli spin matrices

$$\sigma_x = \begin{pmatrix} 0 & 1 \\ 1 & 0 \end{pmatrix} \text{ and } \sigma_y = \begin{pmatrix} 0 & -i \\ i & 0 \end{pmatrix}. \quad (\text{S3})$$

Using this approach, we introduce various perturbations. The deformation of the lattice is given by $\mathbf{U}_{1,2} = \mathbf{U} \pm \mathbf{W}/2$, where the different signs correspond to the different sublattices. This deformation changes the components of the dynamical matrix via $\boldsymbol{\delta}_{\alpha} \rightarrow \tilde{\boldsymbol{\delta}}_{\alpha}$ and $P_{\alpha} \rightarrow \tilde{P}_{\alpha}$, where

$$\tilde{\boldsymbol{\delta}}_{\alpha} = (I + \nabla \mathbf{U}) \boldsymbol{\delta}_{\alpha} \quad (\text{S4})$$

$$\begin{aligned} \tilde{P}_{\alpha} &= P_{\alpha} + (\nabla \mathbf{U}) P_{\alpha} + P_{\alpha} (\nabla \mathbf{U})^T \\ &+ (\mathbf{e}_{\alpha}^T \epsilon \mathbf{e}_{\alpha} + \mathbf{e}_{\alpha}^T \mathbf{W}/a) (I - 3P_{\alpha}) + \mathbf{e}_{\alpha} \mathbf{W}^T/a + \mathbf{W} \mathbf{e}_{\alpha}^T/a, \end{aligned} \quad (\text{S5})$$

and $(\nabla \mathbf{U})_{ij} = \partial_i \mathbf{U}_j$. Substituting these parameters into Eq. (S1) and using perturbation theory, we obtain Eq. (3) of the main text.

In the main text, we discussed those configurations in which the lattice strain results from stress applied only to the boundaries. For such configurations, we imposed the force balance condition within the bulk of the lattice: $\delta U_{tot}/\delta \mathbf{W} = 0$, where U_{tot} is the potential energy associated with each unit cell and is given by

$$U_{tot}(\mathbf{R}) = U_1(\mathbf{R}, \mathbf{R}) + \frac{1}{2} [U_2(\mathbf{R}, \mathbf{R} - \mathbf{a}_2) + U_2(\mathbf{R} + \mathbf{a}_2, \mathbf{R})] \\ + \frac{1}{2} [U_3(\mathbf{R}, \mathbf{R} - \mathbf{a}_1) + U_3(\mathbf{R} + \mathbf{a}_1, \mathbf{R})], \quad (\text{S6})$$

where $U_\alpha(\mathbf{R}_1, \mathbf{R}_2) = \frac{\kappa}{2} (\mathbf{e}_\alpha \cdot [\mathbf{U}_2(\mathbf{R}_2) - \mathbf{U}_1(\mathbf{R}_1)])^2$. Solving the force-balance equation $\delta U_{tot}/\delta \mathbf{W} = 0$ using this energy, we get the result $W_x = \epsilon_{xy}a$ and $W_y = \frac{1}{2}(\epsilon_{xx} - \epsilon_{yy})a$ presented in the main text.

To obtain Eq. (5) of the main text, we insert different spring constants for each of the three springs inside of each unit cell into Eq. (S1) and keep the leading terms in the expansion.

The sublattice-polarized modes

Some of our results for the sublattice-polarized modes can be understood using a connection between mechanical graphene and the Jackiw-Rebbi model [1]. Note that, for the waveguide described in the main text, $\kappa_2 = \kappa_3$ and $V = 0$, which is equivalent to $\delta\kappa_2 = \delta\kappa_3 = -\delta\kappa_1/2 \equiv \kappa\mu$. This case with staggered spring constants along the y -direction is reminiscent of the Su-Schrieffer-Heeger model [2]. Using the formula for the synthetic gauge field in Eq. (3) of the main text, we find the following form for the dynamical matrix:

$$D = D_0 + \frac{1}{3}\omega_0^2\mu(y)\sigma_x. \quad (\text{S7})$$

Thus, we see that the dimensionless parameter μ plays the role of the effective mass in the Jackiw-Rebbi model. For modes of the honeycomb-lattice waveguide near the Dirac frequency, we can obtain the form of the eigenmodes using the zero mode solution of the Jackiw-Rebbi model: $\mathbf{u}(y) \propto \exp[-\int_0^y \mu(y) dy]$. Thus, for the sharp domain wall of Fig. 3, for which the effective mass is a step-function, we find solutions at the domain wall which decay exponentially away from the domain wall. On the other hand, for a mechanical Landau-level mode obtained using material patterning, the mass varies linearly with y , i.e., $\mu \propto y$, and the mode indeed has a Gaussian profile (see Fig. S1). Furthermore, the solutions to the Jackiw-Rebbi model exhibit a parity anomaly, which can be used to ascertain that the domain-wall-bound modes as well as the Landau-level modes are both sublattice-polarized.

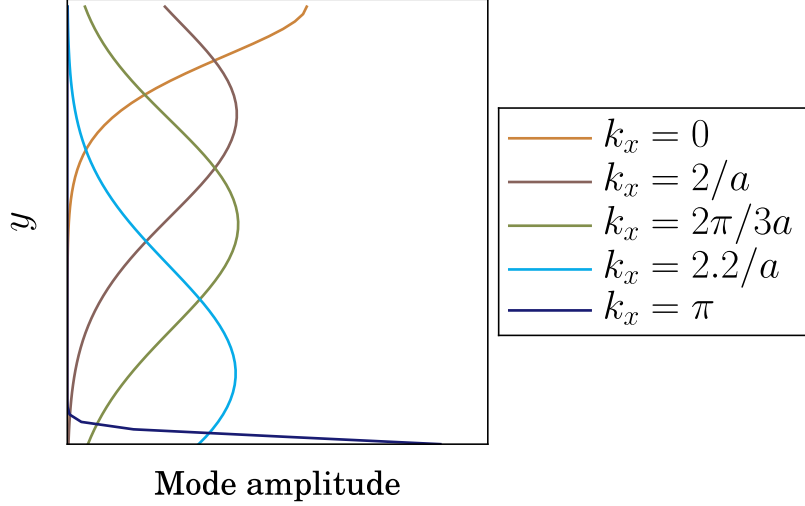


FIG. S1: Visualizations of the zeroth Landau level for different wavenumbers. For $q_x = 2\pi/3a$, this mode has a Gaussian profile and is located precisely at the waveguide center due to a symmetry of the Dirac cone: the modes with frequency above (below) ω_K live on the lower (upper) half of the waveguide. We observe edge states with Gaussian profiles for wavenumber q_x near $2\pi/3a$. For example, when $q_x = 2/a$ (thus $q_x < 2\pi/3a$) the mode has a Gaussian profile and is located near the top edge of the waveguide (brown curve). In contrast, when $q_x = 2.2/a$ (thus $q_x > 2\pi/3a$) the mode has a similar shape, but is located near the bottom edge of the waveguide (light blue curve). Far from the Landau level, at $q_x = 0$ (π), the mode decays exponentially away from the top (bottom) edge. This figure is an expansion of Fig. 2e of the main text.

Topological robustness of the domain-wall mode

In this part, we explain in detail the robustness of the sublattice-polarized domain wall mode in the presence of disorder.

As explained in the main text, a domain wall across which the mass $\mu(y)$ in Eq. (S7) changes sign will always carry a domain-wall-bound mode. Intuitively, this mode corresponds to a Landau-level-like mode but in the presence of a spatially dependent magnetic field given by the derivative $\mu'(y)$. Thus, the existence of the domain-wall bound mode requires μ to change (and, in particular, change in sign) across the domain wall.

One of the consequences of nonzero μ is to break a chiral symmetry in this system. This chiral symmetry preserves the reflection symmetry of the Dirac cone: the cone looks the same right-side up as upside-down. Furthermore, this is the symmetry necessary to

preserve the sublattice polarization (i.e., the fact that the mode lives on only one of the two sublattices) of the domain-wall bound mode. From the fact that μ has to vary across the domain wall and this violation of chiral symmetry, one might suppose that the domain-wall mode's existence also seems to presuppose that it will not be robust against disorder. However, quantitatively, the terms that break this chiral symmetry are small so that the domain-wall modes are nearly perfectly polarized on one sublattice (see Figs. S3 and S4).

Let us first explain the origins of topological robustness in this system and how it relies on chiral symmetry. If the dynamical matrix has form

$$D = \begin{pmatrix} 0 & H \\ H^\dagger & 0 \end{pmatrix}, \quad (\text{S8})$$

then we say that the system does have chiral symmetry. For this dynamical matrix, we can calculate the *winding number* of $\det H$, which is the integral of $\nabla_{\mathbf{k}} \ln \det H$, over a periodic contour γ in the Brillouin zone. The determinant $\det H$ is a complex number for each wavevector, and traces out a closed path in the complex plane as the wavevector follows the contour γ (see Fig. S2b). The integral counts how many times the path encloses the origin $\det H = 0$, and in particular, $\frac{1}{2\pi i} \int_{\gamma} d\mathbf{k} \cdot \nabla_{\mathbf{k}} \ln \det H$ is unity when the origin is enclosed once and zero otherwise. It thus forms a topological invariant for our system, often called the *Herring number* in the context of Dirac cones [3, 4]. Only in the case when the vector potential is zero does this integral become not well-defined, because in that case the contour passes through the center of the Dirac cone, at which point $\det H = 0$.

Notably, in our system, D has the form of Eq. (S8) only near the Dirac cone. Away from points K and K' , chiral symmetry does not hold and other diagonal terms enter the dynamical matrix. However, near the Dirac cone, where all of the phenomena considered in this work take place, these achiral terms are small and the chiral symmetry holds approximately. As a result, the topological robustness associated with this chiral symmetry can also be observed, as we explore in Fig. S4 for the sublattice polarization.

To check that the sublattice polarization remains significant in the presence of system disorder, we have performed numerical simulations of disordered waveguides. In Figure S4 we present the results of these simulations in which we note that although increasing disorder does somewhat affect the sublattice polarization, the effect is small in absolute terms. Even when the disorder strength is around 15% of the initial spring stiffness, the mode remains

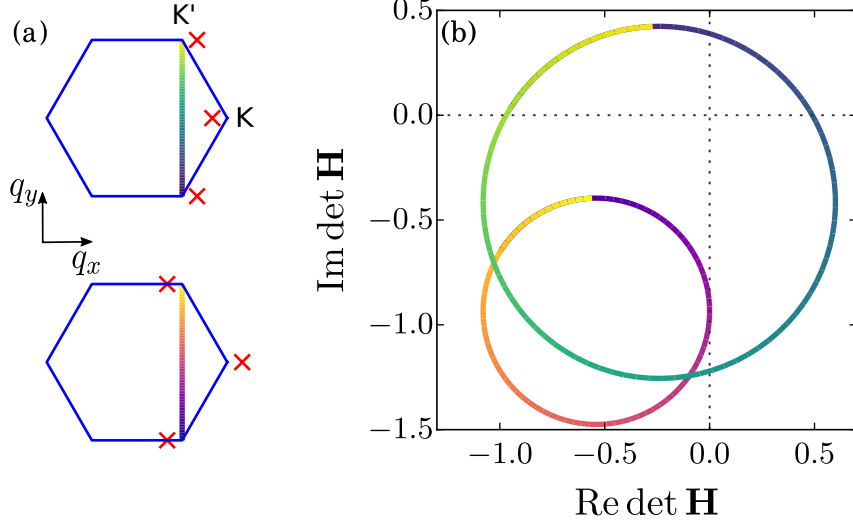


FIG. S2: Topological invariants in a 2D Brillouin zone with a constant gauge field \mathbf{A} . (a) A schematic of the location of the Dirac points when the gauge field is constant. When $\mathbf{A} = (A_x, 0)$ and the x -component A_x is positive, the Dirac cone at \mathbf{q}_K shifts to the left and the cone at $\mathbf{q}_{K'}$ shifts to the right (top panel). For A_x negative, these cones shift in the opposite direction. When the Dirac cones shift, it is possible to define a winding contour around the Dirac cones that connects $\mathbf{q}_{K'}$ with itself via a vertical path across the Brillouin zone. (b) When the quantity $\nabla_{\mathbf{k}} \ln \det H$ [see Eq. (S7)] is integrated along the contour defined in (a), as long as the chiral symmetry of the honeycomb lattice is respected, the resulting quantity is an integer called the Herring number. This number is zero when $A_x > 0$ (small circle, which doesn't enclose the origin) and unity when $A_x < 0$ (large circle, which does enclose the origin). Thus, this number counts the Dirac cones within the contour and can only change when the sign of A_x changes as, e.g., in the case of the Landau level or the domain wall presented in the main text.

polarized within 5% of its initial, near-perfect, polarization.

Selective enhancement

We use the drag matrix $\Gamma = \begin{pmatrix} \gamma \mathbb{I} & 0 \\ 0 & \gamma' \mathbb{I} \end{pmatrix}$ with $\gamma' = 0$ to model sublattice-biased dissipation. With the presence of these drag forces, the equation of motion becomes $m\ddot{\mathbf{u}} + \Gamma\dot{\mathbf{u}} + D\mathbf{u} = 0$. Now consider an external driving force $\mathbf{F}(\mathbf{R}, t) = \mathbf{F}(\mathbf{R})e^{i\omega t}$ which oscillates in time. With this force, the inhomogenous equation of motion is $m\ddot{\mathbf{u}} + \Gamma\dot{\mathbf{u}} + D\mathbf{u} = \mathbf{F}$.

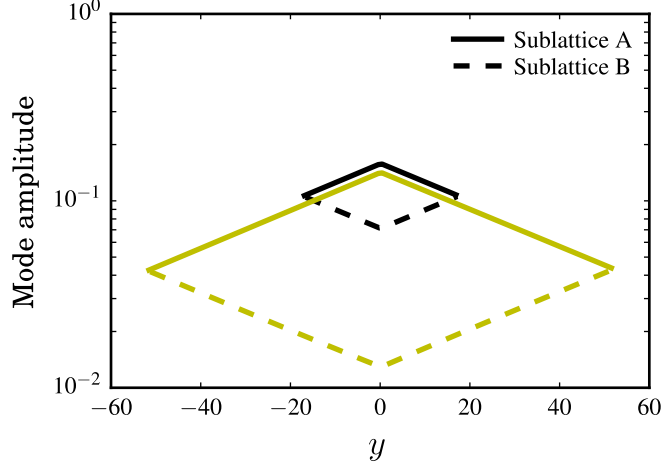


FIG. S3: Amplitude of the midgap mode for quasi-one dimensional waveguides with different sizes $N = 20$ (black) and $N = 60$ (yellow) along the transverse direction plotted on a log-linear scale. For each system size, the amplitude of the vibrational mode on the two sublattices A and B are shown as solid and dashed lines respectively, as a function of y -position relative to the domain wall at $y = 0$. The component on sublattice A decays exponentially away from the domain wall, similar to the exponentially decaying domain-wall mode shown in Fig. 3b of the main text. The mode also has a component on sublattice B, which decays exponentially away from the waveguide edges. This component arises because an edge termination is similar to a domain wall with a different mass sign change compared to the actual domain wall in the system. The relative amplitudes of the two components are set by the boundary conditions at the edges: the loose node condition at the system edge requires that $\mathbf{u}_A = \mathbf{u}_B$, as the nodes at the boundary can not balance a nonzero force from the interior springs.

To find the solutions, we use Bloch functions, i.e., the normal modes of the periodic structure, to expand the drive as $\mathbf{F}(\mathbf{R}, t) = e^{i\omega t} \sum_{\mathbf{n}\mathbf{k}} \mathbf{F}_{\mathbf{n}\mathbf{k}} \mathbf{u}_{\mathbf{n}\mathbf{k}} e^{i\mathbf{k} \cdot \mathbf{R}}$. A steady-state solution, if it exists, oscillates with the same frequency ω as the drive. The steady-state solution can be expanded as $\mathbf{u}(\mathbf{R}, t) = e^{i\omega t} \sum_{\mathbf{k}} c_{\mathbf{n}\mathbf{k}} \mathbf{u}_{\mathbf{n}\mathbf{k}} e^{i\mathbf{k} \cdot \mathbf{R}}$. From the equation of motion, we find that the coefficients $c_{\mathbf{n}\mathbf{k}}$ obey

$$c_{\mathbf{n}\mathbf{k}} = \frac{\mathbf{F}_{\mathbf{n}\mathbf{k}}}{-m\omega^2 + i\Gamma_{\mathbf{n}\mathbf{k}}\omega + \lambda_{\mathbf{n}\mathbf{k}}}, \quad (\text{S9})$$

where $\Gamma_{\mathbf{n}\mathbf{k}} = \sum_{\mathbf{n}'} \mathbf{u}_{\mathbf{n}'\mathbf{k}}^\dagger \Gamma \mathbf{u}_{\mathbf{n}\mathbf{k}}$ and $\lambda_{\mathbf{n}\mathbf{k}}$ are the eigenvalues of the dynamical matrix, Eq. (1) in the main text. We expect the response to depend strongly on the damping. To see this, consider $\Gamma_{\mathbf{n}\mathbf{k}}$ to be a real number. If $\Gamma_{\mathbf{n}\mathbf{k}}^2 > 2\lambda_{\mathbf{n}\mathbf{k}}m$ (corresponding to the overdamped limit),

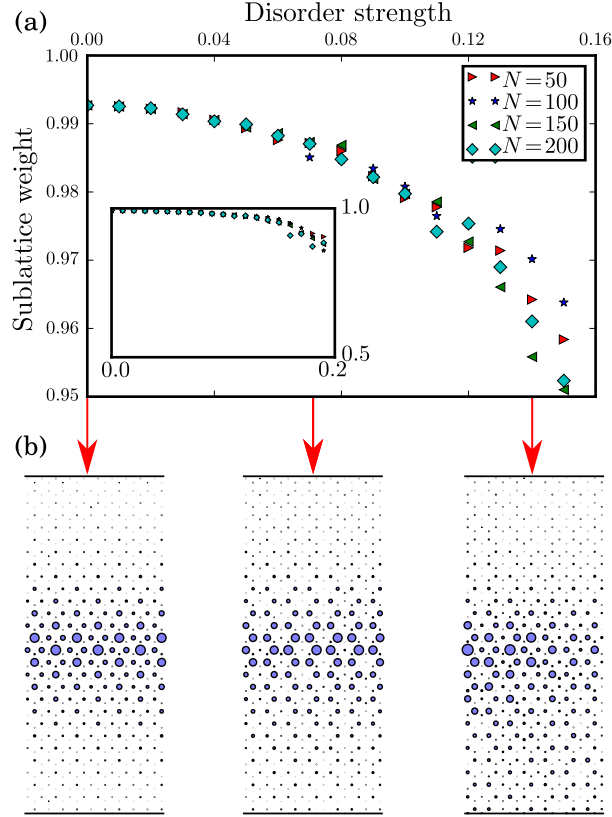


FIG. S4: Effect of disorder in the spring constants on the sublattice polarization of modes bound to domain walls (see Fig. 3 in the main text). (a) We consider waveguides that are infinite along the x -direction and have N unit cells along the y -direction. The disorder is implemented by rescaling each spring constant with spring constant $\kappa + \delta\kappa$ by a random number X via $(1 + X)\kappa + \delta\kappa$, where X is chosen from a uniform distribution on the interval $[-s, s]$ where we call the number s the disorder strength (x -axis of panel a). We then plot the relative weight of each mode on a sublattice averaged over 100 realizations of the disorder in panel (a). We note that it is always near unity (see inset). Even for disorder strength $\sim 10\%$, we note that the modes are still mostly polarized on one sublattice. Even for the most disordered cases we consider, the relative sublattice weight is 0.95, which indicates that the sublattice polarization of the domain-wall bound mode is robust against disorder in the spring constant. (b) Domain-wall bound mode amplitudes on each lattice site for several realizations of the disorder, with different disorder strengths. We note that even in the case in which the effects of the disorder on the mode are appreciable, the mode is still very strongly polarized on one of the sublattices.

then the amplitude of the response never rises above $\mathbf{F}_{n\mathbf{k}}/\lambda_{n\mathbf{k}}$ – it attains this limiting value at low frequencies and falls off as $\mathbf{F}/m\omega^2$ at higher frequencies. If on the other hand, $\Gamma_{n\mathbf{k}}^2 < 2\lambda_{n\mathbf{k}}$ (corresponding to the underdamped limit), the response develops a peak at $\omega_p^2 = \lambda_{n\mathbf{k}}/m - \Gamma_{n\mathbf{k}}^2/2m^2$, whose height diverges as $1/\Gamma_{n\mathbf{k}}$. Therefore, at low damping, the response will be dominated by modes whose natural frequency is close to the driving frequency. If for example, the lattice is driven by forcing atoms along one edge in an oscillatory manner, then $\mathbf{F}_{n\mathbf{k}}$ will be appreciable for several modes, but the only modes to have a strong response will be those whose natural frequency is close to the driving frequency.

This observation can be used to selectively enhance the zeroth Landau level mode, as seen in Fig. 4 of the main text. In Fig. 4a-b, we plot $\chi(\omega) \equiv c_{n\mathbf{k}}/F_{n\mathbf{k}}$ for n corresponding to Landau levels $-2, -1, 0, 1$, and 2 , for $\mathbf{k} = \mathbf{q}_K$. In the insets, we plot the attenuation rates η , corresponding to the imaginary parts of the frequency spectrum, for these modes as a function of \mathbf{k} along the ΓKM cut of the Brillouin zone. For both quantities, the zeroth Landau level mode is selected for nonzero B : it has a stronger response and smaller attenuation than the other modes. We then drive the lattice with force $\mathbf{F}(t) = e^{i\omega t}\hat{x}$ (ω near ω_0), on two of the lattice points (near but slightly above the waveguide center), and observe the amplitude of the steady-state response sufficiently far away from this drive. We note that the Landau-level mode is selectively enhanced.

-
- [1] R. Jackiw and C. Rebbi, Phys. Rev. D **13**, 3398 (1976).
 - [2] W. P. Su, J. R. Schrieffer, and A. J. Heeger, Phys. Rev. Lett. **42**, 1698 (1979).
 - [3] C. Herring, Phys. Rev. **52**, 365 (1937).
 - [4] T. Kariyado and Y. Hatsugai, Sci. Rep. **5**, 18107 (2015).